Lawrence Berkeley National Laboratory

Title

Probing Electric Double-Layer Composition via in Situ Vibrational Spectroscopy and Molecular Simulations

Permalink

https://escholarship.org/uc/item/61t4k2mk

Journal

The Journal of Physical Chemistry Letters, 10(12)

ISSN

1948-7185

Authors

Raberg, Jonathan H
Vatamanu, Jenel
Harris, Stephen J
et al.

Publication Date

2019-06-20

DOI

10.1021/acs.jpclett.9b00879

Peer reviewed

Probing Electric Double-Layer Composition via in Situ Vibrational Spectroscopy and Molecular Simulations

Jonathan H. Raberg,[†,∇] Jenel Vatamanu,[‡,§] Stephen J. Harris,[∥] Christina H. M. van Oversteeg,[⊥]
Axel Ramos,[†] Oleg Borodin,[‡,§] and Tanja Cuk*[,†,#,¶]

[†]Department of Chemistry, University of California, Berkeley, Berkeley, California 94720, United States

[‡]Electrochemistry Branch, Sensor and Electron Devices Directorate, Power and Energy Division, U.S. Army Research Laboratory, Adelphi, Maryland 20783, United States

[§]Joint Center for Energy Storage Research, U.S. Army Research Laboratory, Adelphi, Maryland 20783, United States

[∥]Materials Science Division, Lawrence Berkeley National Laboratory, Berkeley, California 94720, United States

[⊥]Debye Institute for Nanomaterials Science, Utrecht University, 3508 TA Utrecht, The Netherlands

[#]Chemical Science Division, Lawrence Berkeley National Laboratory, Berkeley, California 94720, United States

ABSTRACT: At an electrode, ions and solvent accumulate to screen charge, leading to a nanometer-scale electric double layer (EDL). The EDL guides electrode passivation in batteries, while in (super)capacitors, it determines charge storage capacity. Despite its importance, quantification of the nanometer-scale and potential-dependent EDL remains a challenging problem. Here, we directly probe changes in the EDL composition with potential using in situ vibrational spectroscopy and molecular dynamics simulations for a Li-ion battery electrolyte ($LiClO_4$ in dimethyl carbonate). The accumulation rate of Li^+ ions at the negative surface and ClO_4^- ions at the positive surface from vibrational spectroscopy compares well to that predicted by simulations using a polarizable APPLE&P force field. The ion solvation shell structure and ion-pairing within the EDL differs significantly from the bulk, especially at the negative electrode, suggesting that the common rationalization of interfacial electrochemical processes in terms of bulk ion solvation should be applied with caution.
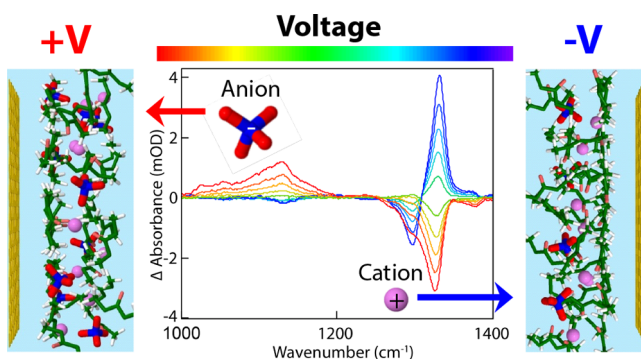
Batteries and electric double-layer capacitors (EDLCs), also called supercapacitors, are commonly utilized as efficient and flexible energy supplies in multiple applications.[1−5] Batteries are well suited for longer-time and steady energy supply while the EDLCs are ideal for short and high bursts of power.[6] Both critical energy storage technologies involve the ubiquitous electric double layer (EDL): a structured, potential-dependent, and nanometer-thin electrolyte layer that screens the electrode charge.

In batteries, the formation of the solid electrolyte interphase (SEI)[7,8] on the negative electrode and the cathode electrolyte interphase (CEI) on the positive electrode[9,10] passivate the electrode surfaces, providing kinetic protection from further electrolyte decomposition. Due to the inherent electrochemical instability of many electrolytes at the lithium, graphite, or silicon anode surfaces, the SEI protective layer enables chemical stability at working voltages beyond the electrolyte's thermodynamic stability at a bare electrode surface. The structure of the initially formed EDL, e.g., in the first battery cycle, impacts the formation of SEI/CEI layers[11−14] because the electrochemical reactions leading to such protective layers depend on the availability of specific species at the surface and their partitioning within the EDL.

Previous simulations[15−17] and experiments[18−22] revealed strongly modulated electrolyte compositions next to the electrode, which influence many ion-related processes, including ion transport, desolvation, charge transfer, and insertion into the electrode. For example, areas within the EDL of increased local ion density will alter interfacial desolvation rates. Further, during the initial steps of SEI formation at the graphite−electrolyte interface, Li ions will either intercalate with a partial solvation shell or shed their solvation shell completely.[23] Both processes are strongly influenced by the ion density and the Li^+ solvation shell composition within the EDL. At the cathode−electrolyte interface, preferential ion and solvent adsorption/desorption were suggested as one of the factors responsible for the

extended electrolyte stability window[24,25] and diminished Al corrosion.[25,26]

Despite the importance of the EDL structure to battery and EDLC operations, progress in its understanding has been limited due to challenges associated with probing a nanometer-scale structure and composition in situ. Previous experiments with atomic force microscopy[20,27] and X-ray reflectivity[21,22] found an EDL structure consisting of several electrolyte layers, while experiments with sum frequency generation spectroscopy identified a pronounced[28,29] innermost Helmholtz-like layer next to the surface. In Li-ion battery electrolytes, the focus of these experiments was largely on the solvent structure within the EDL[30] or the specific adsorption of ions at the surface.[31] Electrochemical quartz crystal microbalance, in situ NMR, and a combination of X-ray scattering and MD simulations yielded the rates of cation and anion adsorption within porous carbon electrodes;[32−34] however, obtaining a detailed EDL composition for open structures has proven difficult. Therefore, despite this significant progress, a quantitative characterization of the individual ions in the EDL has remained a challenging experimental problem, leaving simulations of the strongly modulated electrolyte composition near the electrode without clear corroboration and validation.

Here, we demonstrate that it is possible to advance knowledge of the potential-dependent EDL structure of a battery electrolyte, LiClO$_4$ in dimethyl carbonate (DMC, C$_3$H$_6$O$_3$) solution, by counting the cations (Li$^+$) and anions (ClO$_4^-$) through their associated vibrational spectra. Using attenuated total reflection (ATR) FTIR spectroscopy, an evanescent, interfacial infrared wave probes the vibrations as a function of applied voltage on the electrode. While the evanescent wave penetrates microns into the solution through the thin film electrode and the EDL is nanometer-scale, a difference spectrum with potential accounts for the changes within the EDL that screen the electrode.[35] We show that this in situ vibrational spectroscopy of the EDL can detect the accumulation of Li$^+$ ions at negative voltages and ClO$_4^-$ ions at positive voltages in agreement with predictions from atomistic simulations in the experimentally available potential range. Further, with their validation against (ATR) FTIR experimental results, MD simulations provide important insights into the potential-dependent EDL structure. These insights involve the ion solvation shell structure and the extent of ion-pairing, along with the strongly modulated ion density in the inner Helmholtz layer.

In order to monitor the distribution of Li$^+$ and ClO$_4^-$ near the electrode surfaces by a vibrational probe under applied potential, vibrations associated with the DMC/Li$^+$ complexes and ClO$_4^-$ ions in the bulk electrolyte had to first be identified and quantified for their molar extinction coefficients. Figure 1 shows distinct vibrational stretches of free DMC solvent molecules, DMC coordinated to Li$^+$ ions, and ClO$_4^-$ ions, whose absorption spectra change with LiClO$_4$ concentration. When coordinating to DMC, Li$^+$ weakens the C=O bond of DMC, red-shifting it (Figure 1a) from 1754 to 1723 cm^{-1} in agreement with previous reports.[36,37] However, Li$^+$ coordination of DMC strengthens the ν_{OCO} asymmetric bend of DMC, blue-shifting it from 1278 to 1323 cm^{-1} and the peak grows with increasing LiClO$_4$ concentration (Figure 1b). With increasing LiClO$_4$ concentration, the Li$^+$−DMC peak grows at the expense of free-DMC. DFT calculations described in the Supporting Information (Table S1, Figures S1 and S2) also yield a red shift of the C=O stretch and a blue shift of the
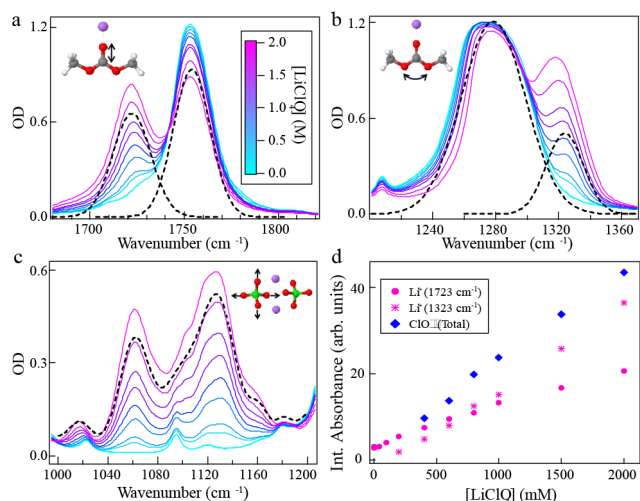

Figure 1. Vibrational stretches associated with Li$^+$ and ClO$_4^-$ ions as a function of [LiClO$_4$] (M) in CO$_3$−(CH$_3$)$_2$ (DMC) solvent: (a) C=O symmetric stretch in free-DMC (1754 cm^{-1}) and Li$^+$ coordinated DMC (1723 cm^{-1}), (b) CO$_3$−R$_2$ symmetric bend in free-DMC (1278 cm^{-1}) and Li$^+$ coordinated DMC (1323 cm^{-1}), and (c) ClO$_4^-$ symmetric stretches, with the two primary frequencies related to ClO$_4^-$ within a CIP. (d) Integrated absorption change associated with [Li$^+$], using the Li$^+$−DMC frequencies of (a) and (b), and [ClO$_4^-$], using the total line shape in (c). The absorption changes scale linearly with [LiClO$_4$] (M), with the reported molar extinction coefficients given in the text.

OCO asymmetric bend of DMC upon Li$^+$ binding to carbonyl oxygen of DMC. The calculated shift magnitudes are similar to experiment, as shown in Table 1, further confirming the

Table 1. Frequencies of Vibrations Associated with Li$^+$ and ClO$_4^-$ Ions in CO$_3$−CH$_3$)$_2$ (DMC) Solvent and Pictured in Figure 1, from FTIR Experiments and DFT Calculations[a]

vibration	ions and solvent	exp (cm^{-1})	DFT (cm^{-1})
$\nu_{C=O}$ stretch	Li$^+$−DMC/free-DMC (shift)	1723/1754 (31)	(35/37)[b]
ν_{OCO} (asym)	Li$^+$−DMC/free-DMC (shift)	1323/1278 (−45)	(−32/−31)[b]
ClO$_4^-$ sym stretch	ClO$_4^-$ in CIP	1098 and 1128	25−29

[a]For ClO$_4^-$, only the primary stretches associated with the CIP are shown. [b]Shifts of DMC frequencies are from PBE/6-31+G(d,p) DFT calculations using DMC(cc)$_3$/LiClO$_4$ and DMC(cc)$_2$DMC(ct)/LiClO$_4$ CIP complexes immersed in implicit solvent.

assignments. Furthermore, DFT calculations show that Li$^+$ binding to DMC noncarbonyl oxygens yield shifts in the opposite direction from the carbonyl oxygen (Figure S1). The former are not observed in IR measurements with increasing salt concentration, confirming that most Li$^+$ bind to the carbonyl oxygen atoms of DMC.

In order to quantify the absorption associated purely with Li$^+$−DMC, the spectra in Figure 1a,b were fit with two Gaussians, representing separately free-DMC and Li$^+$−DMC. In comparison, the vibrational stretches associated with ClO$_4^-$ occur over a broad frequency range between 1160 and 1040 cm^{-1}, where the spectrum is a combination of free ClO$_4^-$ and Li$^+$−ClO$_4^-$ contact-ion pairs (CIP) of various geometries. The absorption over the entire spectral range increases with LiClO$_4$ concentration and accounts for a given number density of
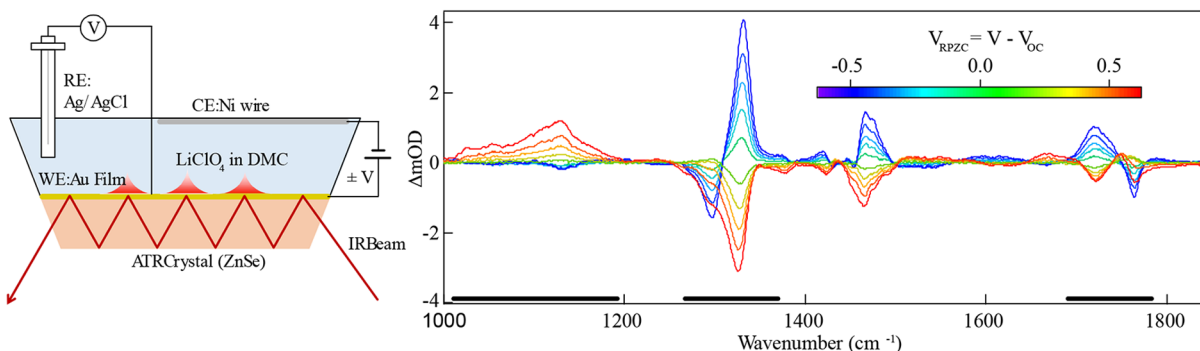
Figure 2. (Left) Attenuated total reflection cell combined with electrochemical control, with an Au thin film working electrode (WE), a wound Ni wire counter electrode (CE), and an Ag/AgCl reference electrode (RE). The number of bounces N in the actual cell is equal to 8. (Right) Absorption change measured for an applied voltage either positive or negative of the open circuit potential (V_{OC}). In this setup, the electrode potential, defined as the potential drop within EDL relative to the potential of zero charge (V_{RPZC}), is the applied voltage V relative to the potential V_{OC}, i.e., $\varphi_{electrode} = V_{RPZC} = V - V_{OC}$. The black bars indicate the three frequency ranges used to extract the $[Li^+]$ and $[ClO_4^-]$ changes as a function of V_{RPZC}.

ClO_4^- ions (Figure 1c). We do not attempt to separate the spectra into the different geometries of CIP, or for the presence of free ClO_4^-, due to both the difficulty in interpreting the broad spectrum and changes to its shape with potential, as will be discussed below.

Nonetheless, DFT calculations showed that the Li^+ binding to ClO_4^- results in the ClO_4^- band being split into two closely positioned blue-shifted peaks and one red-shifted peak as shown in Figure S2 and in agreement with the experimental spectra of Figure 1c. Importantly, the shifts are sensitive to the Li^+ location around the ClO_4^- anion. Thus, we utilized the $DMC(cc)_3-LiClO_4$ and $DMC(cc)_2DMC(ct)-LiClO_4$ complexes with an explicit description of the Li^+ first solvation shell and packing representative of the condensed phase in order to accurately predict shifts of the ClO_4^- bands upon Li^+ complexation, as shown in Figure S1d,e. The two $LiClO_4$ peaks are 25−29 cm^{-1} apart in the DFT calculations, in good agreement with the experimental value of 30 cm^{-1} (see Table 1), which confirms the interpretation of vibrational spectra and suggests that most ClO_4^- anions are bound to a Li^+ as the free ClO_4^- peak at ∼1100 cm^{-1} is very weak, especially at >0.5 M salt concentrations.

The dependence of the absorption changes on $[LiClO_4]$ is used to define three molar extinction coefficients (ε), as shown in Figure 1d, using Beer's law, $A = \varepsilon cl$, where c is the concentration of the species and l is the path length. The evanescent wave produced by an attenuated total reflection (ATR) cell at the ATR crystal/electrolyte interface probes the vibrational spectrum of the electrolyte. For an ATR cell, the path length is defined by $d_{eff}N$ where d_{eff} is the penetration depth of the evanescent wave and N (=8 for ZnSe cell) is the number of times the wave penetrates from the ATR crystal into the electrolyte (see cartoon in Figure 2). The penetration depth of each bounce, d_{eff}, is calculated for the ATR (Ge or ZnSe) crystal/DMC interface (∼1 μm for ZnSe, ∼0.5 μm for Ge, further details are in the Supporting Information). As expected for Beer's law, the integrated absorption spectrum for each species linearly depends on its concentration (Figure 1d). Extinction coefficients are determined by $\varepsilon = m/d_{eff}N$, where m is the slope of the integrated absorption spectrum as a function of $[LiClO_4]$. Two extinction coefficients are thus obtained for Li^+-DMC, from the $C{=}O$ stretch ($\varepsilon_{1723} = 0.00230$ M^{-1} nm^{-1}) and the $CO_3-(CH_3)_2$ ($\varepsilon_{1323} = 0.00376$ M^{-1} nm^{-1})

bend, respectively. However, one extinction coefficient is obtained for ClO_4^- ($\varepsilon_{1160-1040} = 0.00341$ M^{-1} nm^{-1}), which represents a cumulative absorption of the different coordination geometries of ClO_4^-. The full experimental fit procedure used for Figure 1 is described in the Supporting Information, along with Figure S3.

With distinct vibrations and molar extinction coefficients associated with free-DMC, Li^+-MC, and ClO_4^-, we now turn to the potential dependence of the Li^+ and ClO_4^- ion count at an electrode surface. Shown in Figure 2 is the ATR cell used for the in situ electrochemical measurements of the EDL, where a thin film of Au (20 nm) was evaporated on a ZnSe ATR crystal. The working electrode of a three-electrode potentiostat controls the voltage on the Au film with respect to a wound Ni wire and referenced to a custom Ag/AgCl electrode (see Supporting Information). The Au layer had to be thin enough for the evanescent wave to penetrate into the electrolyte, and its thickness was monitored (see Supporting Information for details and Figure S4). The films were composed of nanospheres leading to a 10−20 nm roughness, as seen by SEM, XRD, and AFM (Figure S5 and S6). The differential spectra shown in Figure 2b are obtained by subtracting the spectra at the open circuit (OC) voltage from the spectra with an applied potential. The OC voltage is measured when the Au film is in contact with the electrolyte in a closed cell, but the working electrode is not in direct electrical contact with the counter electrode. To obtain the OC spectra without fluctuations in the environment influencing the data collection, we apply the measured OC voltage ($V = -0.024 \pm 0.04$ V vs SHE) to the working electrode. Absorption changes were obtained for voltages between −0.8 and +0.5 V, chosen to avoid irreversible reactions such as SEI formation. The full experimental procedure is discussed in the Supporting Information (Figure S7−S9). The potential-dependent spectra shown are representative of four trials involving two different Au depositions (Figure S7). The three spectral regions identified in Figure 1 are subject to analysis, with a fourth range left out due to the lack of reproducibility (Figure S9). The frequencies of the vibrations in the potential-dependent spectra are within 5 cm^{-1} of the vibrations of bulk free-DMC and Li^+-DMC spectra (Figure S9, Supplemental Fitting procedure). For ClO_4^-, the vibrations of the potential-dependent spectra occur in the same broad frequency range as

bulk ClO_4^-, although the shape of the broad spectrum differs significantly (Figure 1), which implies changing coordination geometries of ClO_4^- within the EDL. Since the peak frequencies for Li^+-DMC and the frequency range of ClO_4^- agree with the bulk spectra, the potential-dependent changes in these spectral ranges are associated with similar species as in the bulk. We do observe absorption changes not seen in the bulk spectra, and possibly related to chemically adsorbed contaminants; the spectrally broad features of lower intensity seen throughout Figure 2 change for the different trials and in certain cases exhibit distinct Stark effects (Figure S7) where difference spectra are characteristic of electric field induced vibrational frequency shifts. The distinct Stark effects observed correspond to rigid red or blue shifts of the spectrum with potential, which implies they are species that cannot rotate or are fixed to the surface.[38]

The potential dependence of the absorption change (ΔA) describes a redistribution in the EDL due to gain or loss of Li^+-DMC and ClO_4^- near the electrode surface. For voltages negative of OC, ΔA of Li^+-DMC (1723 cm^{-1}, 1323 cm^{-1}) grows more positive, demonstrating an accumulation of Li^+ ions. The opposite occurs for voltages positive of OC, demonstrating a reduction in the number of Li^+ ions. In the ClO_4^- stretch region (1160−1040 cm^{-1}), ΔA markedly increases with voltages positive of OC, demonstrating an accumulation of ClO_4^- ions, while it becomes slightly negative at negative voltages, demonstrating a reduction of ClO_4^- ions. For negative voltages, ΔA of free-DMC grows more negative (1754 cm^{-1}, 1278 cm^{-1}), as Li^+-DMC replaces free-DMC. The positive voltages do not necessarily show the comparable trend of accumulation when free-DMC replaces Li^+-DMC, with varying results between the trials (Figure S7) in this respect.

We quantify the redistribution of Li^+ and ClO_4^- using the molar extinction coefficients identified above. Relating ΔA to ε: $A(V) - A(OC) = \varepsilon[c(V) - c(OC)]d_{eff}N = \varepsilon \Delta c d_{eff}N$, where c represents the ion volume density. Rearranging, $d_{eff} = (1/\varepsilon)\Delta A/N$, where ΔA is the integrated absorption change of the relevant ε cross-section (see Figure S7 for individual fits of the potential-dependent ΔA). $\Delta c d_{eff}$ is the change in the potential-dependent surface ion density ($\Delta n(\varphi)/cm^2$) because d_{eff} accounts for the length of the EDL surface being probed in every bounce (N). $\Delta(\varphi)/nm^2$ is reported as a function of $V_{RPZC} = V_{applied} - V_{OC}$, where the open circuit voltage (V_{OC}) is taken as the potential of the uncharged surface. V_{RPZC} is therefore the potential difference relative to the potential of zero charge (RPZC). The results, shown in Figure 3, quantify the accumulation of ClO_4^- and reduction of Li^+ with positive voltages, and the reduction of ClO_4^- and accumulation of Li^+ with negative voltages, seen in the raw data.

We now turn to the MD simulations, which examined the EDL structure of electrolyte sandwiched between polarizable graphite electrodes using the setup shown Figure S10. The electrode atoms are treated as polarizable utilizing the Siepmann and Reed charge equilibration scheme.[39,40] As in previous work,[40−42] the charges on electrode atoms were Gaussian distributed with widths $\eta^{-1} = 0.5$ Å, which were tuned to reproduce[39,40] the classical electrostatic interactions of charges next to conductor surfaces in vacuum. The electrolyte was modeled with a revised APPLE&P[43] polarizable force-field, having the polarizabilities represented via induced point dipoles dampened with the Thole[44] method. The dialed potential between two electrodes ΔU was varied between 0
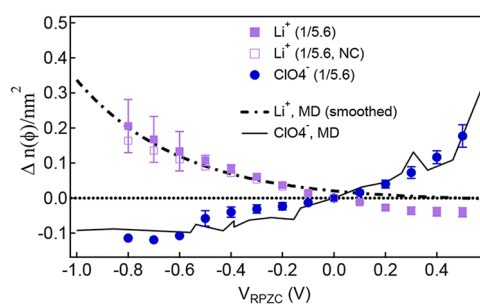

Figure 3. Comparison of MD simulations vs experimentally determined changes in ion number (dotted, Li^+ and line, ClO_4^-) as a function of applied potential for a bulk concentration of 0.8 M. The lines show the fitted interfacial layer densities obtained from MD by integrating the ions density profiles $\rho(z)$ over an interfacial widths of 6 Å from electrode surface. The experimental values for Li^+ (purple squares) and for ClO_4^- (blue circles) are determined by an average of the two Li^+-DMC peaks and the total ClO_4^- line shape, respectively. The Li^+ (open purple squares, NC) are the extracted ion densities considering the calculated changes in the interfacial coordination number of Li^+-DMC. The experimental points were all scaled by $s = 1/5.6$, due to surface enhancement described in the text. The error bars are a standard error over four trials, with only one trial available for voltages lower than −0.5 V. In this region, the two Li^+ were taken as separate trials.

and 3 V. To closely mimic experiments, the electrode potential was calculated relative to bulk electrolyte with a subsequent subtraction of PZC: $V_{RPZC} = V_{electrode} - V_{bulk} - PZC$, where PZC is −0.22 V. Simulation details are summarized in the Supporting Information. During MD simulations, an interfacial structure develops, resulting in formation of several alternating locally rich and depleted layers of ions or solvent, which are most pronounced within ≈10 Å from the surface. The changes in potential of this EDL structure are shown in Figure 4. The laterally averaged density profiles $\langle \rho(z) \rangle$ for ClO_4^- show two pronounced centers of mass peaks centered at 3.7 and 7.2 Å from the surface, which correspond to ClO_4^- populations in the inner Helmholtz and diffuse parts of the EDL respectively. The ClO_4^- population in the inner Helmholtz layer decreases monotonically with negative electrode polarization due to electrostatic repulsion, pushing ClO_4^- anions into the diffuse part of the EDL. The second layer of ClO_4^-, representing the diffuse part of EDL, shows a weak dependence vs voltage (Figure 4a and Figure S11), likely due to strong screening of the electrode charge by the inner layer.

In contrast to the profiles for the center of mass of the ClO_4^- anion, the density profiles for Li^+ tend to be broader (i.e., the first peak is a broad distribution between 4 and 6 Å), and they show less pronounced minima/maxima and dependencies on voltage (Figure 4b). Such behavior of the Li^+ density profiles indicates that in addition to screening electrode charge, the Li^+ cations are also found between layers bridging anions and solvent.[45] It is likely a generic feature because similar broad distributions for the interfacial Li^+ were previously reported for other dilute electrolytes such as $LiPF_6$ in EC:DMC[16] and sulfolane.[46]

Next, we examine changes of the cumulative densities $n(\varphi)$ of the inner Helmholtz layer located within 6 Å from the surface. To compare with experiments, we subtracted the corresponding layer density at the uncharged surface, i.e., $\Delta n(\varphi) = n(\varphi) - n(\varphi = V_{RPZC})$.
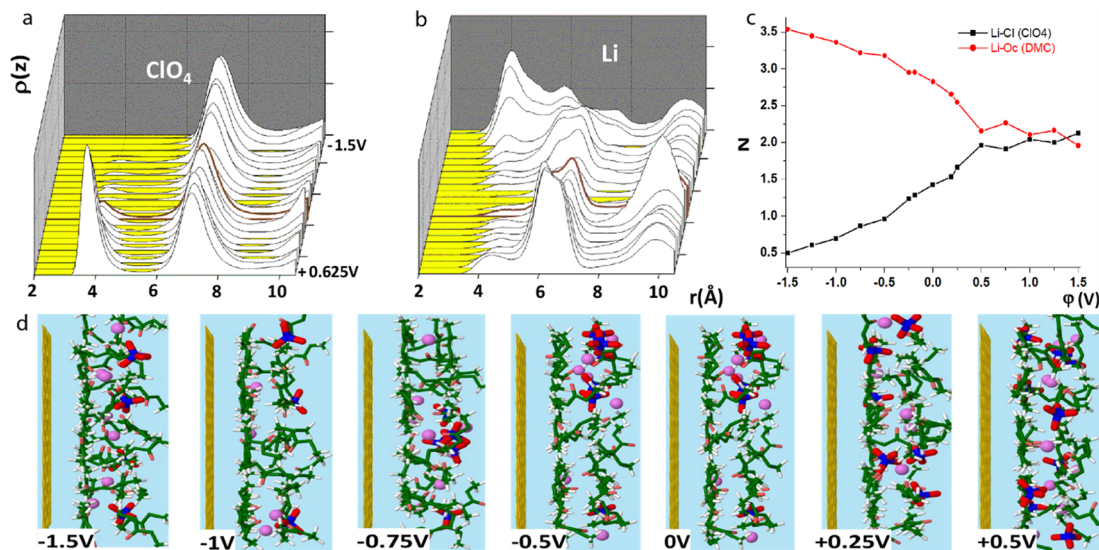
Figure 4. MD simulations of EDL at various electrode potentials. (a) Density profiles of ClO_4^- ions at r distance from the electrode surface. (b) Density profiles of Li^+ ions from the electrode surface. (c) Li^+ coordination numbers. (d) Images of ion densities near the surface.

Shown in Figure 3 are the theoretical curves for the Li^+ and ClO_4^- ion count $(\Delta n(\varphi)/nm^2)$ (solid and dashed lines) on top of the experimental points. In this potential window (≈ -0.8 to $+0.4$ V), both theory and experiments detected a co-ion accumulation and counterion deaccumulation as the surface potential increases. Furthermore, the rate of ion accumulation/deaccumulation is monotonic with potential and agreement between theory and experiment is good. Note that only changes in the innermost interfacial layer (<6 Å) are considered in MD simulations in Figure 3, posing a question regarding the contributions from the second and third interfacial layers and beyond. Figure S12 and S13 show that inclusion of the second and third interfacial layers results in a minor change of the relative interfacial densities, thus indicating that the inner layer adequately represents overall changes of the changes of ion density with potential.

In order to quantitatively assess the simulation results for $n(\varphi)$, comparison with previous work is in order. The extent of charge accumulation vs voltage is often quantified by the half-cell (or electrode) capacitances, i.e., $C = \sigma/\varphi$, where σ is the electrode charge density. Note that the electrolyte excess counter-charge $\Delta n = (n_{Li^+} - n_{ClO_4^-})$ within the EDL is easily available from C or σ, i.e., $\sigma = -\Delta n_{EDL} = -[n_{Li^+} - n_{ClO_4^-}]_{EDL} = -[\Delta n_{Li^+} - \Delta n_{ClO_4^-}]_{EDL}$. We calculated an average capacitance $C_{avg} = \sigma/\varphi$ (or $|\Delta n|/\Delta \varphi$) over a voltage range from ≈ -0.8 to $+0.4$ V where the change in interfacial composition was monotonic. The half-cell C_{avg} from MD was ≈ 4.6 $\mu F/cm^2$ (or $|n_{Li^+} - n_{ClO_4^-}|/\Delta \varphi = 0.262$ (ions/nm^2)/V). The innermost layer had a rate (vs voltage) of charge accumulation $|n_{Li^+} - n_{ClO_4^-}|/\varphi$ equal to 0.32 (ions/nm^2)/V, or 5.2 $\mu F/cm^2$ in units of capacitance. In other words, the innermost layer carries about 20–25% (on average) more charge than the electrode surface (or the entire EDL). Such an overscreening of the innermost layer at these relatively moderate surface voltages is expected from basic classical-DFT theory[47,48] and MD simulations.[49–51] A value for electrode $C_{avg} \approx 4.6$ $\mu F/cm^2$ is in good quantitative agreement with previous simulations of diluted[16,52,53] and superconcentrated[54–56] battery electrolytes. A similar extent of charge increase vs voltage was reported by multiple

simulations[48,57,58] and experiments[59–61] for room temperature ionic liquids.

We now assess the quantitative agreement between experimental and theoretical results. A direct extraction of ion densities $\Delta n(\varphi)/nm^2$ from the voltage-dependent spectra yielded values 5–6 times greater than those found by calculation (Figure 3). Experimental capacitances were also found to be 4–9 times greater than those of the modeled system (Figure S8). One possible explanation for the observed enhancement of both ion densities and capacitance is much higher actual surface area of the sputtered Au due to roughness compared to the nominal cross-section used for normalization of experimental data (Figures S4–6). A second possibility is surface-enhanced infrared absorption. The vibrational cross-section of molecules at a nanometer-scale distance from a rough metal surface can be enhanced, affecting the determination of the ion count. For example, when probing molecules with a mid-infrared ATR evanescent wave through vacuum evaporated metal surfaces of 5–10 nm thickness, the gain can be up to a factor of 10 for nonadsorbed species near the electrode compared to the bulk.[62,63] The origin of the enhancement for nonchemically adsorbed species is understood as an electromagnetic one, of the incident photon exciting the metal surface in concert with the molecules to produce a larger electric field that vibrates them. Since we use the lower, bulk ATR cross-section of the vibrational transitions to extract the ion number densities, $\Delta n(\varphi)/nm^2$ near the electrode is overestimated experimentally. Since the electric-field enhancement occurs as a result of the incident photon exciting the Au surface, it should be agnostic to the species and independent of the electric field within the double layer. While we cannot quantify the relative contributions of these two effects here, their magnitudes align well with our observed enhancement. We should note that differences purely in the ATR evanescent wave intensity, due to changes in the crystal surface or metal coating, could also affect the enhancement factor, though in a more minor way. None of these effects should preferentially enhance one absorber over another, a linear scaling is reasonable. With a scale factor of 1/5.6, a comparison of the resulting experimental ion densities $\Delta n(\varphi)/$

nm^2 with calculation generated good agreement for the rates of ion accumulation with potential ($\Delta n(\varphi)/\Delta \varphi$) (Figure 3) and, as detailed above, these charging rates are in accord with previous theoretical work.

During extraction of the Li$^+$ accumulation curves from vibrational spectra it was assumed that accumulation of the DMC complexed by Li$^+$ is proportional to accumulation of Li$^+$. This assumption, however, might not hold if the number of DMC coordinating Li$^+$ at the electrode surfaces changes with potential. Therefore, we examined changes of the interfacial Li$^+$ coordination numbers, as shown in Figure 4c. At the most negatively polarized electrode, the Li$^+$ cations are the most dissociated from anions and are mostly coordinated by DMC. As the electrode becomes positively polarized up to 0.5 V, the number of anions coordinating a Li$^+$ cation increases with a corresponding decrease in the number of DMC molecules coordinating Li$^+$. We note that such a potential-dependent coordination number only slightly modifies the ion count, as shown in Figure 3; the curve Li$^+$ (NC) extracts the ion densities from experiment considering the changes the interfacial Li$^+$ coordination numbers imply for the extinction coefficient. However, Figure 4c provides an important observation because the Li$^+$ coordination number is commonly probed in bulk electrolytes and yet is often related to interfacial processes.[64,65] Our MD simulations, verified by their good agreement with the potential dependence of the experimental ion count, suggest that this approach should be applied with caution due to differences between the interfacial and bulk solvation.

Finally, one needs to consider that the DMC vibrational band ν_{OCO} (asym) decreases in intensity while the $\nu_{C=O}$ band increases in intensity when DMC is complexed to Li$^+$ and this effect is somewhat dependent on the DMC conformation (see Table S1 in the Supporting Information). Since the average values of $\Delta n(\varphi)/nm^2$ reported by these two modes are utilized to extract the final Li$^+$ ion count, the errors due to increased/decreased IR intensities resulting from changes in DMC conformation should be partially canceled.

We showed that in situ attenuated total reflection vibrational spectroscopy of a battery electrolyte can count the ion density within the EDL. This information is important for understanding energy storage in EDLCs and provides additional insight for critical processes in batteries, such as desolvation or formation of the SEI and CEI. More generally, the results show that a true molecular description of reactants, solvent, and ions near an electrode surface can be obtained by the combination of in situ vibrational spectroscopy and MD simulations, which is relevant not only to batteries but also to any electrochemical process utilized for fuel generation or chemical synthesis.

■ EXPERIMENTAL METHODS

The spectroelectrochemical cell was designed and built in house with polyether ether ketone (PEEK) plastic and sealed vacuum-tight with polytetrafluoroethylene (PTFE) O-rings. A high surface-area counter electrode (CE) was constructed of wound Ni wire. The reference electrode (RE) was a Ag/AgClO$_4$ redox couple in propylene carbonate (20 mM AgClO$_4$, 1.0 M LiClO$_4$). The potential of the RE was measured to be 3.666 V with respect to lithium metal (0.626 vs SHE) in 1.0 M LiClO$_4$/PC and was stable to ±1 mV over a 33 h period.

The working electrode (WE) was prepared by thermal evaporation of gold (5 × 10^{-6} Torr, 0.1 nm/s) onto a ZnSe ATR crystal (20 × 50 mm, 45°, Spectral Systems). The evaporated Au is vulnerable to physical abrasion at the O-ring seals of the electrochemical cell. We therefore evaporated an additional binding layer of 1−2 nm of Cr at the crystal edges. No Cr was used in the region in contact with the electrolyte. The thickness of the gold film was measured by UV−vis (Shimadzu UV-2600) to be 39 ± 2 nm (with the exception of the first trial, which had a thickness of 26 nm). Scanning electron microscopy (JEOL JSM 634OF) showed the gold to have a nanoparticle-like surface layer. X-ray diffraction (Siemens D500 Diffractometer, Cu Kα emission) revealed these to be Au(111) crystallites with a diameter of 14 ± 1 nm. Atomic force microscopy confirmed a smooth (RMS ∼ 1 nm) surface layer comprised of nanoparticle-like gold with diameters of 10−20 nm.

The electrolytes were prepared and the spectroelectrochemical cell assembled under a nitrogen atmosphere. All chemicals were anhydrous and purchased at the highest purity available. IR spectra were taken in an ATR geometry at 2 cm^{-1} resolution under a continuously purged nitrogen atmosphere using a Bruker Vertex 70 V spectrometer with an external, LN$_2$-cooled, mercury cadmium telluride detector. Electrochemical methods were conducted with a CH Instruments 1140B potentiostat. The spectrometer and potentiostat were controlled and coordinated using software created in Lab-VIEW.

The general structure of the experiment was as follows. First, a voltage of 0 V with respect to the open circuit potential (∼0.1 V vs SHE) was applied. The current was allowed to stabilize over a wait period of 15 s, after which 15 scans were taken over a period of 31 s. Next, the voltage was switched to some target voltage V, and the same wait and scan parameters were applied. Finally, the initial voltage was reapplied and the cycle repeated until enough spectra were collected to satisfy signal-to-noise constraints. The spectra were then subtractively normalized and averaged. This method of rapid voltage switching helped to eliminate experimental artifacts and drifts.

A concentration calibration (0−2.0 M LiClO$_4$/DMC) was performed using a bare Ge crystal in an ATR geometry. Spectra were fit with Gaussian peaks (Igor Pro), and molar extinction coefficients were calculated. Voltage-dependent SNIFTIRS peaks were subsequently fit in the same way and EDL concentrations were calculated using the extinction coefficients. The wavelengths in the SNFITIRS spectra were allowed to vary slightly from those in the bulk (±5 cm^{-1} for Li$^+$---DMC peaks and ±11 cm^{-1} for ClO$_4^-$). A surface enhancement factor of 5× was incorporated into the data to bring the results into agreement with theory.

■ ASSOCIATED CONTENT

ⓢ Supporting Information

Experimental and theoretical methods, DFT table of vibrational frequencies, pictures of DMC/Li$^+$ complexes, dependence of the ClO$_4^-$ anion vibrational band on the Li···O−Cl bending angle, concentration calibration with linear fits, bulk spectral calibrations of the extinction coefficients, surface characterization of evaporated films, different experimental trials of the potential dependent vibrational spectra, experimental capacitance, fitting

procedure for potential dependent vibrational peaks and extracted ion densities with potential, cell for molecular dynamics simulations, theoretical ion density profiles, and the full calculated range of main manuscript Figure 3 (PDF)

■ AUTHOR INFORMATION

Corresponding Author

*E-mail: tanja.cuk@colorado.edu.

ORCID ⊕

Jenel Vatamanu: 0000-0003-0825-1608

Christina H. M. van Oversteeg: 0000-0002-5634-684X

Oleg Borodin: 0000-0002-9428-5291

Tanja Cuk: 0000-0002-1635-2946

Present Addresses

∇Department of Geological Sciences and Institute of Arctic and Alpine Research (INSTAAR), University of Colorado, Boulder, CO.

¶Department of Chemistry and Renewable and Sustainable Energy Institute (RASEI), University of Colorado, Boulder, CO.

Author Contributions

The manuscript was written through contributions of all authors. All authors have given approval to the final version of the manuscript.

Notes

The authors declare no competing financial interest.

■ REFERENCES

(1) Tarascon, J.-M.; Armand, M. Issues and challenges facing rechargeable lithium batteries. *Mater. Sustainable Energy* **2010**, 171−179.

(2) Scrosati, B.; Garche, J. Lithium batteries: Status, prospects and future. *J. Power Sources* **2010**, *195*, 2419−2430.

(3) Blomgren, G. E. The Development and Future of Lithium Ion Batteries. *J. Electrochem. Soc.* **2017**, *164*, A5019−A5025.

(4) Salanne, M.; Rotenberg, B.; Naoi, K.; Kaneko, K.; Taberna, P. L.; Grey, C. P.; Dunn, B.; Simon, P. Efficient storage mechanisms for building better supercapacitors. *Nat. Energy* **2016**, *1*, 16070.

(5) Tarascon, J. M.; Armand, M. Issues and challenges facing rechargeable lithium batteries. *Nature* **2001**, *414*, 359−367.

(6) Thounthong, P.; Raël, S.; Davat, B. Energy management of fuel cell/battery/supercapacitor hybrid power source for vehicle applications. *J. Power Sources* **2009**, *193*, 376−385.

(7) Peled, E. The Electrochemical Behavior of Alkali and Alkaline Earth Metals in Nonaqueous Battery Systems—The Solid Electrolyte Interphase Model. *J. Electrochem. Soc.* **1979**, *126*, 2047−2051.

(8) Andersson, A. M.; Edström, K. Chemical Composition and Morphology of the Elevated Temperature SEI on Graphite. *J. Electrochem. Soc.* **2001**, *148*, A1100−A1109.

(9) Liu, Y.-M.; Nicolau, B. G.; Esbenshade, J. L.; Gewirth, A. A. Characterization of the Cathode Electrolyte Interface in Lithium Ion Batteries by Desorption Electrospray Ionization Mass Spectrometry. *Anal. Chem.* **2016**, *88*, 7171−7177.

(10) Lu, W.; Zhang, J.; Xu, J.; Wu, X.; Chen, L. In Situ Visualized Cathode Electrolyte Interphase on LiCoO2 in High Voltage Cycling. *ACS Appl. Mater. Interfaces* **2017**, *9*, 19313−19318.

(11) Browning, J. F.; Baggetto, L.; Jungjohann, K. L.; Wang, Y.; Tenhaeff, W. E.; Keum, J. K.; Wood, D. L.; Veith, G. M. In Situ Determination of the Liquid/Solid Interface Thickness and Composition for the Li Ion Cathode LiMn1.5Ni0.5O4. *ACS Appl. Mater. Interfaces* **2014**, *6*, 18569−18576.

(12) Fears, T. M.; Doucet, M.; Browning, J. F.; Baldwin, J. K. S.; Winiarz, J. G.; Kaiser, H.; Taub, H.; Sacci, R. L.; Veith, G. M. Evaluating the solid electrolyte interphase formed on silicon electrodes: a comparison of ex situ X-ray photoelectron spectroscopy and in situ neutron reflectometry. *Phys. Chem. Chem. Phys.* **2016**, *18*, 13927−13940.

(13) Veith, G. M.; Doucet, M.; Sacci, R. L.; Vacaliuc, B.; Baldwin, J. K.; Browning, J. F. Determination of the Solid Electrolyte Interphase Structure Grown on a Silicon Electrode Using a Fluoroethylene Carbonate Additive. *Sci. Rep.* **2017**, *7*, 6326.

(14) Owejan, J. E.; Owejan, J. P.; DeCaluwe, S. C.; Dura, J. A. Solid Electrolyte Interphase in Li-Ion Batteries: Evolving Structures Measured In situ by Neutron Reflectometry. *Chem. Mater.* **2012**, *24*, 2133−2140.

(15) Vatamanu, J.; Borodin, O. Ramifications of Water-in-Salt Interfacial Structure at Charged Electrodes for Electrolyte Electrochemical Stability. *J. Phys. Chem. Lett.* **2017**, *8*, 4362−4367.

(16) Vatamanu, J.; Borodin, O.; Smith, G. D. Molecular Dynamics Simulation Studies of the Structure of a Mixed Carbonate/LiPF6 Electrolyte near Graphite Surface as a Function of Electrode Potential. *J. Phys. Chem. C* **2012**, *116*, 1114−1121.

(17) Feng, G.; Huang, J.; Sumpter, B. G.; Meunier, V.; Qiao, R. Structure and dynamics of electrical double layers in organic electrolytes. *Phys. Chem. Chem. Phys.* **2010**, *12*, 5468−5479.

(18) Steinrück, H.-G.; Cao, C.; Tsao, Y.; Takacs, C. J.; Konovalov, O.; Vatamanu, J.; Borodin, O.; Toney, M. F. The nanoscale structure of the electrolyte−metal oxide interface. *Energy Environ. Sci.* **2018**, *11*, 594−602.

(19) Yamamoto, R.; Morisaki, H.; Sakata, O.; Shimotani, H.; Yuan, H.; Iwasa, Y.; Kimura, T.; Wakabayashi, Y. External electric field dependence of the structure of the electric double layer at an ionic liquid/Au interface. *Appl. Phys. Lett.* **2012**, *101*, 053122.

(20) Zhang, X.; Zhong, Y.-X.; Yan, J.-W.; Su, Y.-Z.; Zhang, M.; Mao, B.-W. Probing double layer structures of Au (111)-BMIPF6 ionic liquid interfaces from potential-dependent AFM force curves. *Chem. Commun.* **2012**, *48*, 582−584.

(21) Mezger, M.; Ocko, B. M.; Reichert, H.; Deutsch, M. Surface layering and melting in an ionic liquid studied by resonant soft X-ray reflectivity. *Proc. Natl. Acad. Sci. U. S. A.* **2013**, *110*, 3733−3737.

(22) Nishi, N.; Uruga, T.; Tanida, H.; Kakiuchi, T. Temperature Dependence of Multilayering at the Free Surface of Ionic Liquids Probed by X-ray Reflectivity Measurements. *Langmuir* **2011**, *27*, 7531−7536.

(23) Xu, K.; von Cresce, A.; Lee, U. Differentiating Contributions to "Ion Transfer" Barrier from Interphasial Resistance and Li+ Desolvation at Electrolyte/Graphite Interface. *Langmuir* **2010**, *26*, 11538−11543.

(24) Vatamanu, J.; Borodin, O. Ramifications of Water-in-Salt Interfacial Structure at Charged Electrodes for Electrolyte Electrochemical Stability. *J. Phys. Chem. Lett.* **2017**, *8*, 4362−4367.

(25) Borodin, O.; Ren, X.; Vatamanu, J.; von Wald Cresce, A.; Knap, J.; Xu, K. Modeling Insight into Battery Electrolyte Electrochemical Stability and Interfacial Structure. *Acc. Chem. Res.* **2017**, *50*, 2886−2894.

(26) McOwen, D. W.; Seo, D. M.; Borodin, O.; Vatamanu, J.; Boyle, P. D.; Henderson, W. A. Concentrated electrolytes: decrypting electrolyte properties and reassessing Al corrosion mechanisms. *Energy Environ. Sci.* **2014**, *7*, 416−426.

(27) Zhong, Y.-X.; Yan, J.-W.; Li, M.-G.; Zhang, X.; He, D.-W.; Mao, B.-W. Resolving Fine Structures of the Electric Double Layer of Electrochemical Interfaces in Ionic Liquids with an AFM Tip Modification Strategy. *J. Am. Chem. Soc.* **2014**, *136*, 14682−14685.

(28) Baldelli, S. Surface Structure at the Ionic Liquid−Electrified Metal Interface. *Acc. Chem. Res.* **2008**, *41*, 421−431.

(29) Xu, S.; Xing, S.; Pei, S.-S.; Ivaništšev, V.; Lynden-Bell, R.; Baldelli, S. Molecular Response of 1-Butyl-3-Methylimidazolium Dicyanamide Ionic Liquid at the Graphene Electrode Interface Investigated by Sum Frequency Generation Spectroscopy and Molecular Dynamics Simulations. *J. Phys. Chem. C* **2015**, *119*, 26009−26019.

(30) Yu, L.; Liu, H.; Wang, Y.; Kuwata, N.; Osawa, M.; Kawamura, J.; Ye, S. Preferential Adsorption of Solvents on the Cathode Surface of Lithium Ion Batteries. *Angew. Chem.* **2013**, *125*, 5865−5868.

(31) Borodin, O.; Ren, X.; Vatamanu, J.; von Wald Cresce, A.; Knap, J.; Xu, K. Modeling Insight into Battery Electrolyte Electrochemical Stability and Interfacial Structure. *Acc. Chem. Res.* **2017**, *50*, 2886−2894.

(32) Futamura, R.; Iiyama, T.; Takasaki, Y.; Gogotsi, Y.; Biggs, M. J.; Salanne, M.; Ségalini, J.; Simon, P.; Kaneko, K. Partial breaking of the Coulombic ordering of ionic liquids confined in carbon nanopores. *Nat. Mater.* **2017**, *16*, 1225.

(33) Griffin, J. M.; Forse, A. C.; Tsai, W.-Y.; Taberna, P.-L.; Simon, P.; Grey, C. P. In situ NMR and electrochemical quartz crystal microbalance techniques reveal the structure of the electrical double layer in supercapacitors. *Nat. Mater.* **2015**, *14*, 812−819.

(34) Tsai, W.-Y.; Taberna, P.-L.; Simon, P. Electrochemical Quartz Crystal Microbalance (EQCM) Study of Ion Dynamics in Nanoporous Carbons. *J. Am. Chem. Soc.* **2014**, *136*, 8722−8728.

(35) Pons, S. The use of fourier transform infrared spectroscopy for in situ recording of species in the electrode-electrolyte solution interphase. *J. Electroanal. Chem. Interfacial Electrochem.* **1983**, *150*, 495−504.

(36) Chapman, N.; Borodin, O.; Yoon, T.; Nguyen, C. C.; Lucht, B. L. Spectroscopic and Density Functional Theory Characterization of Common Lithium Salt Solvates in Carbonate Electrolytes for Lithium Batteries. *J. Phys. Chem. C* **2017**, *121*, 2135−2148.

(37) Borodin, O.; Olguin, M.; Ganesh, P.; Kent, P. R. C.; Allen, J. L.; Henderson, W. A. Competitive lithium solvation of linear and cyclic carbonates from quantum chemistry. *Phys. Chem. Chem. Phys.* **2016**, *18*, 164−175.

(38) Chattopadhyay, A.; Boxer, S. G. Vibrational Stark Effect Spectroscopy. *J. Am. Chem. Soc.* **1995**, *117*, 1449−1450.

(39) Siepmann, J. I.; Sprik, M. Influence of surface topology and electrostatic potential on water/electrode systems. *J. Chem. Phys.* **1995**, *102*, 511−524.

(40) Reed, S. K.; Lanning, O. J.; Madden, P. A. Electrochemical interface between an ionic liquid and a model metallic electrode. *J. Chem. Phys.* **2007**, *126*, 084704.

(41) Vatamanu, J.; Borodin, O.; Smith, G. D. Molecular dynamics simulations of atomically flat and nanoporous electrodes with a molten salt electrolyte. *Phys. Chem. Chem. Phys.* **2010**, *12*, 170−182.

(42) Kiss, P. T.; Sega, M.; Baranyai, A. Efficient Handling of Gaussian Charge Distributions: An Application to Polarizable Molecular Models. *J. Chem. Theory Comput.* **2014**, *10*, 5513−5519.

(43) Borodin, O. Polarizable Force Field Development and Molecular Dynamics Simulations of Ionic Liquids. *J. Phys. Chem. B* **2009**, *113*, 11463−11478.

(44) Thole, B. T. Molecular polarizabilities calculated with a modified dipole interaction. *Chem. Phys.* **1981**, *59*, 341−350.

(45) Borodin, O.; Smith, G. D. Development of Many−Body Polarizable Force Fields for Li-Battery Applications: 2. LiTFSI-Doped Oligoether, Polyether, and Carbonate-Based Electrolytes. *J. Phys. Chem. B* **2006**, *110*, 6293−6299.

(46) Xing, L.; Vatamanu, J.; Borodin, O.; Smith, G. D.; Bedrov, D. Electrode/Electrolyte Interface in Sulfolane-Based Electrolytes for Li Ion Batteries: A Molecular Dynamics Simulation Study. *J. Phys. Chem. C* **2012**, *116*, 23871−23881.

(47) Bazant, M. Z.; Storey, B. D.; Kornyshev, A. A. Double Layer in Ionic Liquids: Overscreening versus Crowding. *Phys. Rev. Lett.* **2011**, *106*, 046102.

(48) Feng, G.; Huang, J.; Sumpter, B. G.; Meunier, V.; Qiao, R. A "counter-charge layer in generalized solvents" framework for electrical double layers in neat and hybrid ionic liquid electrolytes. *Phys. Chem. Chem. Phys.* **2011**, *13*, 14723−14734.

(49) Sha, M.; Dou, Q.; Luo, F.; Zhu, G.; Wu, G. Molecular Insights into the Electric Double Layers of Ionic Liquids on Au(100) Electrodes. *ACS Appl. Mater. Interfaces* **2014**, *6*, 12556−12565.

(50) Hu, Z.; Vatamanu, J.; Borodin, O.; Bedrov, D. A comparative study of alkylimidazolium room temperature ionic liquids with FSI and TFSI anions near charged electrodes. *Electrochim. Acta* **2014**, *145*, 40−52.

(51) Feng, G.; Qiao, R.; Huang, J.; Dai, S.; Sumpter, B. G.; Meunier, V. The importance of ion size and electrode curvature on electrical double layers in ionic liquids. *Phys. Chem. Chem. Phys.* **2011**, *13*, 1152−1161.

(52) Haskins, J. B.; Wu, J. J.; Lawson, J. W. Computational and Experimental Study of Li-Doped Ionic Liquids at Electrified Interfaces. *J. Phys. Chem. C* **2016**, *120*, 11993−12011.

(53) Haskins, J. B.; Lawson, J. W. Evaluation of molecular dynamics simulation methods for ionic liquid electric double layers. *J. Chem. Phys.* **2016**, *144*, 184707.

(54) McEldrew, M.; Goodwin, Z. A. H.; Kornyshev, A. A.; Bazant, M. Z. Theory of the Double Layer in Water-in-Salt Electrolytes. *J. Phys. Chem. Lett.* **2018**, *9*, 5840−5846.

(55) Yang, H.; Yang, J.; Bo, Z.; Chen, X.; Shuai, X.; Kong, J.; Yan, J.; Cen, K. Kinetic-Dominated Charging Mechanism within Representative Aqueous Electrolyte-based Electric Double-Layer Capacitors. *J. Phys. Chem. Lett.* **2017**, *8*, 3703−3710.

(56) Li, Z.; Jeanmairet, G.; Méndez-Morales, T.; Rotenberg, B.; Salanne, M. Capacitive Performance of Water-in-Salt Electrolytes in Supercapacitors: A Simulation Study. *J. Phys. Chem. C* **2018**, *122*, 23917−23924.

(57) Feng, G.; Li, S.; Atchison, J. S.; Presser, V.; Cummings, P. T. Molecular Insights into Carbon Nanotube Supercapacitors: Capacitance Independent of Voltage and Temperature. *J. Phys. Chem. C* **2013**, *117*, 9178−9186.

(58) Si, X.; Li, S.; Wang, Y.; Ye, S.; Yan, T. Effects of Specific Adsorption on the Differential Capacitance of Imidazolium-Based Ionic Liquid Electrolytes. *ChemPhysChem* **2012**, *13*, 1671−1676.

(59) Uesugi, E.; Goto, H.; Eguchi, R.; Fujiwara, A.; Kubozono, Y. Electric double-layer capacitance between an ionic liquid and few-layer graphene. *Sci. Rep.* **2013**, *3*, 1595.

(60) Druschler, M.; Borisenko, N.; Wallauer, J.; Winter, C.; Huber, B.; Endres, F.; Roling, B. New insights into the interface between a single-crystalline metal electrode and an extremely pure ionic liquid: slow interfacial processes and the influence of temperature on interfacial dynamics. *Phys. Chem. Chem. Phys.* **2012**, *14*, 5090−5099.

(61) Siinor, L.; Arendi, R.; Lust, K.; Lust, E. Influence of temperature on the electrochemical characteristics of Bi(111) ionic liquid interface. *J. Electroanal. Chem.* **2013**, *689*, 51−56.

(62) Metiu, H. Surface Enhanced Spectroscopy. *Prog. Surf. Sci.* **1984**, *17*, 153−320.

(63) Hatta, A.; Ohshima, T.; Suetaka, W. Observation of the enhanced infrared absorption of p-nitrobenzoate on Ag island films with an ATR technique. *Appl. Phys. A: Solids Surf.* **1982**, *29*, 71−75.

(64) von Cresce, A.; Xu, K. Preferential Solvation of Li$^+$ Directs Formation of Interphase on Graphitic Anode. *Electrochem. Solid-State Lett.* **2011**, *14*, A154−A156.

(65) Fan, X.; Chen, L.; Ji, X.; Deng, T.; Hou, S.; Chen, J.; Zheng, J.; Wang, F.; Jiang, J.; Xu, K.; Wang, C. Highly Fluorinated Interphases Enable High-Voltage Li-Metal Batteries. *Chem.* **2018**, *4*, 174−185.